



1

2

3

4

5



Stratified-turbulence observations in the deep Mediterranean

7

8

9

10

11

by Hans van Haren

12

13

14

15

16

17

18

19

20

21 Royal Netherlands Institute for Sea Research (NIOZ), P.O. Box 59, 1790 AB Den Burg,
22 the Netherlands.

23

e-mail: hans.van.haren@nioz.nl

24

25



26 **Abstract.** A nearly half-cubic hectometer of deep Mediterranean-Sea waters is yearlong sampled with
27 about 3000 high-resolution temperature sensors to study different sources of turbulent waterflows,
28 which are vital for life. Although temperature differences are never larger than 0.01°C, daily, weekly,
29 and seasonal variations are observed. About half the time, relatively warm stratified waters are moved
30 from 100's of meters higher levels to near the seafloor. These internal-wave and sub-mesoscale eddy-
31 induced motions are half an order of magnitude more turbulent than those induced via general
32 geothermal heating from below, and about one order of magnitude more turbulent than those from open-
33 ocean processes. A rough estimate shows that eddy-induced stratified turbulence is likely more
34 important for deep-sea life than rare, not observed, deep dense-water formation at the abyssal-plain
35 mooring site. With a delay of about a week, the stratified turbulence tracks atmospheric disturbances,
36 which are found 35% more energetic in winter than in summer. From comparison of turbulence-
37 calculation methods, of band-pass filtering with vertical-displacement reordering, for data over one-four
38 days, a generalization is proposed for the filter cut-offs under weakly stratified and near-homogeneous
39 conditions in the deep Mediterranean.

40



41 **1 Introduction**

42 Irreversible, energy-consuming turbulence is indispensable for life on earth, also in the deep sea. Most
43 ocean turbulence is generated near its boundaries, with an important input via the breaking of internal
44 waves at steeply sloping underwater topography (Eriksen, 1982; Thorpe, 1987). Observational details
45 are still scarce from the abyssal deep sea that is commonly considered to be ‘quiescent and stagnant’.
46 One of the key aspects in the breaking of internal waves is the ‘warming phase’, when, e.g., an internal
47 tide moves downslope and characteristically (re-)stratifies waters near the seafloor with near-
48 homogeneous waters due to convection turbulence above. Less known are slantwise-moving, warm
49 turbulent waters possibly related with near-inertial waves and (sub-)mesoscale eddies in basins like the
50 Mediterranean Sea where tides and stratified conditions are both weak. As will be demonstrated in this
51 paper, these warm waters have the potential to generate larger turbulent mixing than in the open-ocean
52 interior.

53 Under weakly stratified conditions, the potential of deep-sea turbulence generation via downward or
54 slantwise moving waters should be compared with local general geothermal heating ‘GH’ through the
55 seafloor (e.g., Pasquale et al., 1996), and with deep dense-water formation ‘DWF’ from the surface (e.g.,
56 Marshall and Schott, 1999). Sparse shipborne microstructure profiling has provided estimates of
57 turbulence contributions from different sources across the Northwestern Mediterranean in which GH is
58 found more important than internal wave breaking (Ferron et al., 2017). However, details of relevant
59 processes are lacking and require high-resolution moored observations over prolonged periods of time.

60 In a stably-stratified environment like the sun-heated ocean, downward motions of warm water seem
61 impossible in relation with irreversible convection turbulence involving motion in three spatial
62 dimensions ‘3D’. Natural, body-forced buoyancy-driven convection (e.g., Dalziel et al., 2008; Ng et al.,
63 2016) applies to denser waters moving down and less dense waters moving up in narrow plumes, i.e. in
64 terms of temperature variations: warmer waters moving up and cooler waters moving down. In the
65 ocean, such buoyancy-driven convection turbulence occurs regularly in the upper O(10) m near the
66 surface during nighttime (e.g., Brainerd and Gregg, 1995) and possibly lower 100 m above the seafloor
67 due to GH, depending on the local stratification. It can also occur as DWF after specific preconditioning
68 of stratification reduction near the surface in localized areas like polar seas and the Mediterranean during



69 brief irregular, rare periods (Marshall and Schott, 1999). An exemption can occur when the other major
70 contributor to density variations dominates over temperature variations: if downward moving warm
71 waters are sufficiently saltier than their environment, cooler and fresher waters may move up.

72 A reversible, also 3D, process occurs when internal-wave motions affect the stratified environment
73 (e.g., LeBlond and Mysak, 1978). Such motions may displace relatively warm waters downward during
74 a particular wave-phase, and cooler waters up. However, such displacements will not overturn and
75 vertically mix the different water masses.

76 A combination of irreversible and reversible processes was observed in fresh-water alpine Lake
77 Garda, where in the weakly stratified waters underneath internal waves convection turbulence was
78 observed (van Haren and Dijkstra, 2021). As these observations showed similarity with the warming
79 phase of a nonlinear wave breaking above a sloping seafloor (e.g., van Haren and Gostiaux, 2012), it
80 was suggested that the convection underneath internal waves was either generated via shear moving
81 convection tubes slantwise, or via wave-accelerations overcoming vertical density differences in
82 internal-forcing overcoming reduced gravity, instead of body-forcing overcoming gravity as in natural
83 convection. Similar to the effect of large-scale shear, planetary slantwise convection in the direction of
84 the Earth's rotational vector may be brought about by the horizontal Coriolis parameter f_h (Marshall and
85 Schott, 1999). The convection can be induced via resonantly-forced standing inertial waves under
86 homogeneous conditions (McEwan, 1973). At mid-latitudes, apparently-stable stratification having
87 buoyancy frequencies of $N = f_h, 2f_h$ or $4f_h$ occur in marginal stability due to planetary slantwise
88 convection (van Haren, 2008).


89 In this paper, we further pursue the investigation of downward convective warm-water periods
90 inducing stratified-turbulence that occur frequently in the deep Western Mediterranean. For this
91 purpose, a nearly half-cubic-hectometer large 3D mooring-array is constructed holding about 3000 high-
92 resolution temperature T-sensors and deployed at a deep seafloor. Turbulence calculations are made for
93 a full observational year to investigate potential seasonal variations. Of the governing physics processes
94 that indirectly may affect deep-sea life by inducing or transporting sufficient turbulence for nutrient and
95 oxygen supply are: atmospheric-disturbance generated near-inertial waves, boundary-flow instability
96 generating sub-, $O(1)$ km, and meso-, $O(10-100)$ km, scale eddies. Motions associated with these



97 processes dominate dispersal of water masses in seas and oceans. While they are not considered to be
98 part of irreversible ‘small-scale’ turbulent mixing, they are all greatly affected by the rotation of the
99 Earth. How they transfer energy to small-scales of turbulence dissipation is not yet fully established.
100 The large number of independent T-sensors is expected to improve statistics of turbulence values, in an
101 environment where all dynamics is captured by temperature variations of less than 0.01°C. The small
102 temperature variations put a large strain on the technical capabilities of quantifying the deep-sea
103 turbulence.

104

105 **2 Materials and Methods**

106  In order to get some insight in the generation and development of deep-sea turbulence, 2925
107 independent, self-contained high-resolution NIOZ4 temperature ‘T’-sensors were distributed in nearly
108 half-a-million cubic meters of seawater. With two supplementary T-sensors registering tilt information
109 above and below, 63 T-sensors were taped at 2-m intervals to 45 vertical lines 125-m tall that each were
110 tensioned to 1.3 kN by a single buoy on top. The T-sensors were located between nominally $h = 1.5$ -
111 125.5 ± 0.5 m above seafloor and recorded data at a rate of once per 2 s. Three buoys, of lines 1.4, 3.5
112 and 5.7 (henceforth throughout the text, the original naming ‘group.line’ is shortened without period;
113 for layout see Appendix A1), held a single-point Nortek AquaDopp current meter ‘CM’ at $h = 126$ m,
114 which recorded data once per 600 s. The lines were attached at 9.5-m horizontal intervals to a steel-
115 cable grid that was tensioned inside a 70-m diameter steel-tube ring functioning as a 140-kN anchor.
116 The ensemble ‘large-ring mooring’ was deployed on the $< 1^\circ$ flat and 2458-m deep seafloor of 42°
117 49.50°N , $006^\circ 11.78^\circ\text{E}$ just 10 km south of the steep continental slope, 5 km from its abyssal-plain foot,
118 of the Northwestern Mediterranean Sea, in October 2020 (Fig. 1a). At the site’s (mid-)latitude $f_h = 1.08f$.
119 Details of construction and deployment of the large-ring mooring can be found in van Haren et al.
120 (2021). For calibration and reference purposes, a single shipborne Conductivity Temperature Depth
121 ‘CTD’ profile was obtained to $h = 0.5$ m, about 1 km horizontally from the mooring site during the
122 deployment cruise.




123 With the aid of Irish Marine Institute Remotely Operated Vehicle (ROV) “Holland I” all 45 vertical
124 lines with T-sensors were successfully recovered in March 2024. Of the lines, 43 were mechanically in
125 good order. Line 18 was hit by the drag parachute, which functioned as a stabiliser during the free-fall
126 deployment, whereby 10 sensors were lost. Line 65 was about 0.5-m lower than nominal because of a
127 loop near the cable grid. Fig. A1 shows the numbering of the lines, which were ordered in six groups
128 for synchronisation purposes. As with previously deployed NIOZ4 T-sensors (for details see van Haren,
129 2018), the individual clocks were synchronised to a single standard clock every 4 hours, so that all T-
130 sensors were sampled within 0.02 s. Line 36 did not register synchronization, possibly due to an electric
131 cable failure. Three T-sensors leaked and <10 were shifted in position due to a tape malfunctioning.
132 After calibration, some 20 extra T-sensors are not further considered due to electronics (noise) problems.
133 In total, 2882 out of 2925 T-sensors functioned as expected for the first 20 months after deployment,
134 with remaining bias due to electronic drift resulting in deviations from absolute accuracy. Depending
135 on the period and type of analysis considered, between 50 and 150 T-sensors showed too large bias
136 requiring additional attention during post-processing of the records from the weakly stratified deep sea.

137 Due to unknown causes all T-sensors switched off unintentionally when the file size on the memory
138 card reached 30 MB. This may have to do with a formatting or programming error. It implied that a
139 maximum of 20 months of data was obtained.

140 With respect to previous NIOZ4 T-sensor version, improvements of the electronics resulted in about
141 ~~twice lower~~ noise levels of 0.00003°C and ~~twice longer~~ battery life. As described in van Haren (2018),
142 calibration yielded a relative precision of <0.001°C. Bias due to instrumental electronic drift of <
143 0.001°C mo⁻¹ after aging was primarily corrected by referencing daily averaged vertical profiles, which
144 must be stable from a perspective of turbulent overturning in a stratified environment, to a smooth
145 polynomial without instabilities. In addition, because vertical temperature (density) gradients are so
146 small in the deep Mediterranean, reference was made to periods of typically one hour duration that were
147 homogeneous with temperature variations smaller than instrumental noise level (van Haren, 2022). Such
148 periods were on days 350, 453, and 657 in the existing records. This secondary correction included low-
149 pass noise filtering ‘lpf’ of data with time. Under near-homogeneous conditions, a tertiary correction



150 involved lpf of data in the vertical. Temperature records were pressure-corrected by transferring to
151 Conservative Temperature Θ (IOC et al., 2010) using CTD's mean local salinity value. Henceforth, Θ
152 will be named 'temperature', for short.

153  Given the consistent and tight temperature-density relationship (Section 3), corrected temperature
154 data allowed for calculations of turbulence values using the overturning displacement method of Thorpe
155 (1977) by reordering density instabilities. Here, the method is applied under weakly stratified conditions
156 in which buoyancy frequency $N \ll 10f$, f denotes the local inertial frequency. For the present deep-sea
157 area, distinction is made between periods under environmental conditions when $N \sim f$, somewhat
158 exaggerating named stratified-water 'SW' conditions, and $N \sim f$ including unstable values, named near-
159 homogeneous 'NH' conditions. For NH, the tertiary correction is needed, and, when unstable overturns
160 exceed the 124-m vertical range of sensors, an extra correction is mandatory because the Thorpe (1977)
161 method of reordering is over-estimating displacements and resulting stratification (van Haren, 2025).
162 Such periods are difficult to trace, because of the extremely small vertical temperature differences, and
163 the selection can only be done manually as it is inadequately automated.

164 For comparison with mean Thorpe (1977) method, turbulence values are also computed using
165 'Ellison'-scales (Ellison, 1957 for atmospheric data; Itsweire, 1984 for laboratory data; Moum, 1996 for
166 oceanographic microstructure profiler data). Such scales are determined from moored T-sensor time
167 series by filtering out internal wave and sub-mesoscale motions. The method is quite sensitive for the
168 precise high-pass filter 'hpf' cut-off frequency, as was noted for well-stratified Atlantic Ocean waters
169 (Cimatoribus et al., 2014 for oceanographic moored T-sensor data). ~~Here in Appendix A2, a modified~~
170 ~~version for application to moored T-sensor data under very weakly stratified conditions is proposed and~~
171 filter cut-off frequencies are given for SW and NH conditions in the deep Mediterranean. For both
172 methods, mean values are obtained from moored multiple-line T-sensor records after averaging over at
173 least the largest turbulence scales, over the vertical '[...]', over time '<...>', and over 45 horizontally
174 distributed lines '(...)'.
175
176
177



178 **3 Results**

179 The focus is on the first full year of observations to investigate potential seasonal variation in deep-sea
180 **turbulence values**. The yearlong data-overview time series in Fig. 2 demonstrates 2-30 day variations,
181 in waterflow speed (Fig. 2a), temperature (Fig. 2b), horizontal velocity difference (Fig. 2c), and vertical
182 temperature difference (Fig. 2d). Such time-variability is typical for sub-meso- and mesoscale motions,
183 which are likely associated with the dynamically unstable, meandering boundary current over the
184 canyon-incised steep continental slope (Crepon et al., 1982) and which may develop into eddies.

185 Over the one year of observations, the waterflow speed U seldom exceeds 0.1 m s^{-1} , with little
186 variations through the seasons. U also rather strongly varies with local inertial period, which partially
187 **reflects the variable thickness of the graphical curves** in Fig. 2a.

188 **Inertial motions do not dominate T-sensor data** (Fig. 2b,d). Also in contrast with U , the T -data
189 demonstrate a seasonal variation with relatively warmer (Fig. 2b) and more stratified (Fig. 2d) waters in
190 winter, coarsely between days 365 and 495. The entire dynamical temperature variation over the year
191 and up to $h = 125 \text{ m}$ from the seafloor is captured within maximum $|\Delta\Theta| < 0.01^\circ\text{C}$, and commonly
192 amounts only a few millidegrees. About half the time, $\Delta\Theta > 0.0002^\circ\text{C} \equiv T_{\text{thres}}$, a threshold level that is
193 about six times the standard deviation of T -sensor noise level and which provides an overall
194 stratification resulting in $N > 0.65f$. These relatively warm SW either come from above or from the side.
195 The other half of the time $\Delta\Theta < T_{\text{thres}}$, $N < 0.65f$ and stratification may be unstable, or NH conditions.
196 Under NH, less than 0.7% of total time negative temperature differences are found exceeding the
197 (absolute value of) threshold level and corresponding with large-scale, >125-m developed GH. As a
198 result, at the observational site convection turbulence associated with GH is suppressed by warm waters
199 advected into the area most of the time.

200 Although the boundary current is strongest near the surface, it manifests itself at great depths
201 including mesoscale variations at horizontal scales $O(10-100) \text{ km}$. However, observed spatial waterflow
202 variations over about 50-m horizontally indicate much smaller-scale, rapidly-fluctuating differences
203 (Fig. 2c). These variations associate, in absolute value, with warm SW conditions in approximately half
204 the cases. No cooling, inversely stratified waters, from above are observed in the yearlong record.



205 Compared to open-ocean waters where large 100-m scale $N > 10f$, the deep Mediterranean SW are
206 characterized by weak stratification with $N = O(f)$. Despite the relatively weak stratification, SW will
207 prove important for turbulent mixing in the area.

208 The single shipborne CTD observations show no dominant influence of salinity over temperature
209 governing density variations, in the lower 500 m above the seafloor (Fig. 3). Over the well-resolved
210 stratified portion between $-2165 < z < -2055$ m, the density-temperature relationship is found to be
211 consistent (cf. van Haren, 2025),

$$212 \quad \delta\sigma_2/\delta\Theta = -0.25 \pm 0.01 \text{ kg m}^{-3} \text{ }^\circ\text{C}^{-1}, \quad (1)$$

213 where $\delta\sigma_2$ denotes the density anomaly referenced to a pressure level of 2×10^7 Pa. Hence, Θ can be used
214 as tracer for density variations to quantify turbulent overturning using the Thorpe (1977) method.

215 In the weakly stratified waters over a vertical range of 100 m, density stratification varies, so that N
216 $< 1f$ or NH is found near the seafloor, and $N \approx 2f$ or SW around $z = -2050$ m (Fig. 3d). Over 25-m
217 vertical ranges, $N \geq 2f$ can be found (Fig. 3d), and over 1-10 m ranges $N > 4f$ may be inferred from Fig.
218 3c around $z = -2110$ and -1980 m. Such thin stratified layers are occasionally also found at greater depths
219 if the better-resolved temperature profile is investigated (Fig. 3b). While the occasional vertical
220 temperature differences of $< 0.01^\circ\text{C}$ in Fig. 2d could result from horizontal differences or fronts, it seems
221 more likely that stratification of around $z = -2050$ m in Fig. 3 is periodically lowered by action from
222 above. Such action is expected down to about $h < 10$ m from the seafloor, a thin layer in which vertical
223 temperature differences are generally very small but not always (black graph in Fig. 2d).

224 Thus, although the moored T-sensors were located between the seafloor and $z = -2332$ m, CTD-
225 measured stratification may vary considerably with depth and time, and physical processes may lower
226 warmer water some 400 m or advecting such waters slantwise, or possibly quasi-horizontally into the
227 range of T-sensors. The precise direction of warm-water motion cannot be determined from single-
228 station profiles, but may be resolved with a properly scaled 3D mooring-array.

229

230

231



232 **3.1 1D-details of an arbitrary warm-water period**

233 Considering an average 5-mK-amplitude warm-water period (cf. Fig. 2b), a 1.3-day depth-time detail
234 from around day 485 is presented from single line 15 (Fig. 4). While waters seem depressed from $h >$
235 125 m, the warming occurs in variable periods of <1 hour (Fig. 4a). During the second half of the
236 warming, 0.001°C additional heat is observed near the top. Relatively warm waters reach the seafloor
237 twice within an inertial period of 0.73 day, around days 485.45 and 485.80. The warming ends with two
238 cooler-water fronts and large overturning reaching the seafloor around day 486.2.

239 The warming is depressed to within $h < 10$ m from the seafloor, with a relatively large vertical
240 temperature gradient between the cooler waters near the seafloor and the warmer waters higher up. This
241 is reflected in the increased value of 2-m-small-scale buoyancy frequency N_s in $h < 30$ m. Turbulent
242 overturns hardly occur between days 485.2 and 486.15 for $h < 5$ m, but are non-negligible in the stratified
243 waters above for $5 < h < 30$ m, and are typically 50-m large further up for $h > 30$ m (Fig. 4b).

244 Quantifying turbulence dissipation rate requires averaging, over all overturning scales possible, and
245 124-m vertically averaged values demonstrate variations with time over two orders of magnitude, when
246 reordered data are used (Thorpe (1977) method, black graph in Fig. 4c), or using $48 < \omega < 3000$ cpd
247 (cycles per day) band-pass filtered data (Ellison (1957) method cf. Appendix A2, cyan graph in Fig. 4c).

248 Time-depth mean values for line 15 from SW's day 485 are: turbulence dissipation rate $\langle[\varepsilon_T]\rangle =$
249 $6\pm 3\times 10^{-10} \text{ m}^2\text{s}^{-3}$ and turbulent diffusivity $\langle[K_z]\rangle = 1.5\pm 0.7\times 10^{-3} \text{ m}^2\text{s}^{-1}$ under buoyancy frequency $\langle[N]\rangle$
250 $= 2.9\pm 0.3\times 10^{-4} \text{ s}^{-1} \approx 3f$, using Thorpe (1977) method. Modified Ellison (1957)-method $\langle[\varepsilon_E]\rangle = 7\pm 3\times 10^{-}$
251 $^{10} \text{ m}^2\text{s}^{-3}$ (Appendix A2). These turbulence values are more than one order of magnitude larger than open-
252 ocean values observed in stratified waters well away from boundaries (e.g., Gregg, 1989; Polzin et al.,
253 1997; Yasuda et al., 2021).

254

255 **3.2 1D-details of an arbitrary near-homogeneous period**

256 For comparison, such turbulence values are under NH conditions between days 316.5 and 320.5 (Fig.
257 5): $2\pm 1\times 10^{-10} \text{ m}^2\text{s}^{-3}$ and $1.1\pm 0.5\times 10^{-2} \text{ m}^2\text{s}^{-1}$ under buoyancy frequency $\langle[N]\rangle = 0.5\pm 0.2\times 10^{-4} \text{ s}^{-1} = 0.5f$.
258 These values follow partially correcting the original method by Thorpe (1977) for overturns exceeding
259 the height of instrumentation with information from manually selected NH environments that are



260 bounded by stratification above (van Haren, 2025). For periods with NH bounded by stratification
261 above, such as between days 318.6 and 318.96, their mean turbulence dissipation rate is to within 10%
262 the same as found for periods with convection turbulence due to GH: $\epsilon_{GH} = 1.2 \times 10^{-10} \text{ m}^2\text{s}^{-3}$. The ϵ_{GH}
263 matches average geophysical heat-flux observations in the area (Pasquale et al., 1996), under the
264 condition that the mixing coefficient of $\Gamma_C = 0.5$ (van Haren, 2025), which is typical for buoyancy-
265 driven convection turbulence (Dalziel et al., 2008). For this period, $\langle[\epsilon_E]\rangle = 1.3 \pm 1 \times 10^{-10} \text{ m}^2\text{s}^{-3}$
266 (Appendix A2).

267

268 **3.3 Some 45-line statistics of short periods under SW and NH conditions**

269 For consistency and statistics, six half-day periods are considered for computation of turbulence
270 dissipation rate values, three under SW and three under NH conditions. The computations are performed
271 for all 45 vertical lines and averages are computed over the 124-m height and half-day periods. It
272 provides a one-and-a-half order of magnitude distribution of mean turbulence dissipation rate values
273 (Fig. 6).

274 While some values are highly consistent between lines, e.g. the most energetic period on day 441,
275 others show a half-order of magnitude distribution of values like on day 459. Initially, this calculation
276 was set-up to help identify biased T-sensors and the appropriate polynomial correction. After applied
277 tertiary correction, remaining wide distributions are attributed to more general turbulence variability.

278 The statistics certainly improve turbulence dissipation rate values calculated using other
279 instrumentation and methodology, which is generally to within a factor of two at best. The six examples
280 of 45 lines provide about four times better statistics for the half-day periods (Table 1). The three NH
281 values average to $\langle[\epsilon_T]\rangle_{NH} = 1.1 \pm 0.2 \times 10^{-10} \text{ m}^2\text{s}^{-3}$, which is well within error equivalent to ϵ_{GH} for $\Gamma_C =$
282 0.5 , while significantly different from the value for $\Gamma_C = 0.2$. It thus confirms previous results (van
283 Haren, 2025) and laboratory findings for convection-turbulence (e.g., Dalziel et al., 2008). The three
284 SW values average to $\langle[\epsilon_T]\rangle_{SW} = 8 \pm 5 \times 10^{-10} \text{ m}^2\text{s}^{-3}$, noting that the standard deviation of individual mean
285 values are one order of magnitude smaller.



286 Another consequence of the use of multiple mooring lines besides improved statistics, is some insight
287 in possible distribution of mean turbulence values. While one would expect erratic distribution over the
288 short horizontal distances <70 m, particularly NH distributions yield two-dimensional consistent images
289 such as on days 459 and 495 (Fig. 7). It provides confidence in consistency of methods used, but results
290 in a puzzling gradient in turbulence that apparently is independent of waterflow (measured at $h = 126$
291 m). For these GH- and near-inertial eddies-dominated periods the 9.5-m interval between lines seems
292 reasonably well chosen, where 100 m may have been too large.

293

294 3.4 Yearlong daily averaged turbulence for 45 lines

295 A yearlong time series of daily-averaged turbulence values is computed for all 45 lines (Fig. 8). This
296 computation is automated, using a fixed 3rd-order polynomial for primary correction. Since the tertiary
297 correction for >125-m extending overturns is not applied manually, a criterion for excluding such
298 episodes is applied. The criterion is simply based on the daily-averaged temperature difference between
299 uppermost and lowest T-sensor, per line. When $\Delta\Theta < T_{\text{thres}}$, given previously, the daily and vertical mean
300 dissipation rate is fixed to,

$$301 \quad \langle[\varepsilon_T]\rangle = \varepsilon_{\text{GH}} = 1.2 \times 10^{-10} \text{ m}^2 \text{ s}^{-3}, \quad (3)$$

302 the mean value for geothermal heating (van Haren, 2025). This is found to occur in $59 \pm 1.5\%$ of the time,
303 somewhat varying per line, and characterizes NH, besides GH. About $40 \pm 1.5\%$ of the time is
304 characterized by SW.

305 The overall, yearlong, 125-m vertical, and 45-line mean turbulence dissipation rate amounts,

$$306 \quad \langle\langle[\varepsilon_T]\rangle\rangle = 2.4 \pm 0.2 \times 10^{-10} \text{ m}^2 \text{ s}^{-3}, \quad (4)$$

307 so that the mean SW turbulence dissipation rate amounts,

$$308 \quad \langle\langle[\varepsilon_T]\rangle\rangle_{\text{SW}} = 4.3 \pm 0.4 \times 10^{-10} \text{ m}^2 \text{ s}^{-3}, \quad (5)$$

309 which is thus closely represented by the short periods of days 308 and 485 in Fig. 6, Table 1.

310 Part of the SW-turbulence is attributable to GH in a layer of typically $h = 30$ m under stratified waters.
311 This may be inferred from the vertical temperature difference in that layer that passes T_{thres} during only
312 8% of daily periods, cf. the magenta graph in Fig. 2d. Nevertheless, the advection of warmer waters



313 suppresses GH-turbulence, possibly affecting the small-scale distribution in Fig. 7, and the associated
314 3.5-times larger turbulence dissipation rates (5) are induced by convection and more generally by shear
315 following internal-wave breaking.

316 Considering the yearlong ‘seasonal’ variation that was suggested from the temperature (difference)
317 time series in Fig. 2, and which is represented by the logarithm of daily and vertically averaged $\langle[N]\rangle$
318 in Fig. 8c, the corresponding plot of $\langle[\varepsilon_T]\rangle$ (Fig. 8b) is more difficult to interpret, also in conjunction
319 with meteorological data (Fig. 8a). Different-line data mostly collapse on each other during winter
320 between days 365 and 495, for both $\langle[N]\rangle$ and $\langle[\varepsilon_T]\rangle$. During this period, vertical-line daily mean
321 turbulence dissipation rates most, 27 out of 41, exceed twice the mean value (4), shown by the green
322 asterisks in Fig. 8a. The 11% of time of green-asterisks occurrence average to a mean turbulence
323 dissipation rate of $7 \times 10^{-10} \text{ m}^2 \text{ s}^{-3}$.

324 The average turbulence dissipation rate for the 130-day winter period is 25% higher than the yearlong
325 mean (4). During this period, the wind work $\sim W^2$ is increased by 20% compared to its yearlong average
326 value. A rough visual correspondence is found between $|W|$ (Fig. 8a) and $\lg\langle[\varepsilon_T]\rangle$ (Fig. 8b), the former
327 leading the latter by about one week. The clearest value-collapse of turbulence and stratification data
328 from different lines is found between days 450 and 500. The early-spring period is unlikely governed
329 by deep DWF due to limited meteorological forcing (Fig. 8a), but the preceding winter cooling may
330 induce enhanced sub-mesoscale activity. Although increased sub-mesoscale motions can obscure near-
331 inertial internal waves (van Haren and Millot, 2003), the transfer of energy to internal-wave scales
332 leading to breaking and turbulence is not hampered. Possibly, as near-inertial shear is dominant in well-
333 stratified waters, a shift from shear to convection turbulence may be associated with the increase of sub-
334 mesoscale activity. Such potential energy transfer will be elaborated elsewhere.

335 In contrast, 14% lower mean turbulence dissipation rate than (4) is found during the summer between
336 days 540-670. In this period, W^2 is decreased by 13% compared to its yearlong average value.

337

338

339



340 **4 Discussion and conclusions**

341 The observations show short $O(10)$ day periods of typically 0.005°C warmer waters than their
342 environment appearing from above, but also, as inferred from the 3D mooring-array, from the sides. The
343 periods occur at a coarse near-inertial periodicity, which is much less deterministic than a tide, and at
344 twice the inertial periodicity. Like internal waves in the Atlantic and Lake Garda (van Haren and
345 Dijkstra, 2021), they push stratification to within a few meters from the seafloor. The pushdown is
346 vigorously turbulent, more than one order of magnitude larger than in the open ocean away from
347 boundaries. This relatively large turbulence should not surprise as both the bulk Reynolds number
348 $O(10^6)$ and buoyancy Reynolds number $\varepsilon/(vN^2) = O(10^4)$ are large, even in the weakly stratified deep
349 sea. The $\nu \approx 10^{-6} \text{ m}^2 \text{ s}^{-1}$ denotes the kinematic viscosity. As GH is found to be relatively weaker, the
350 convection turbulence seems to be driven by the, slanted, internal waves from above.

351 While vertical motions by wintertime DWF have been observed via moored observations (e.g.,
352 Schott et al., 1996) and floats (Steffen and D'Asaro, 2002), and surface buoyancy fluxes have been
353 estimated to be $O(10^{-7}) \text{ m}^2 \text{ s}^{-3}$ during convection events (Marshall and Schott, 1999), quantification via
354 observations of turbulence values associated with DWF reaching the abyssal seafloor have yet to be
355 made (Thorpe, 2005). Unfortunately, a dense-water event never reached the large-ring mooring while it
356 was underwater. Estimates of deep-convection duration are limited, albeit that some consensus exists
357 about decadal variability or occurrence of seafloor-reaching DWF over a relatively short period of (less
358 than) a week (Lilly et al., 1999), maximum a month, per 8-10 years (Dickson et al., 1996; Mertens and
359 Schott, 1998). It is tempting to compare coarse DWF turbulence estimates with GH and SW turbulence
360 calculated from observations at the present mooring site.

361 Because of the lack of measurements to quantify DWF turbulence, some insight is gained from
362 **nocturnal convection-turbulence near the ocean surface**. Microstructure measurements by, e.g., Brainerd
363 and Gregg (1995) demonstrated turbulence dissipation rate values $> 10^{-7} \text{ m}^2 \text{ s}^{-3}$ close to the surface and
364 which decreased in the $O(10)$ m near-homogeneous layer to typically,

365 $\varepsilon_{\text{DWF}} \approx 10^{-8} \text{ m}^2 \text{ s}^{-3},$ (6)



366 at a depth just above well-stratified waters below. The one order of magnitude reduced value reflects
367 the erosion of the stratification. Here, we take value (6) as a proxy for dissipation rate by an event of
368 DWF-convection turbulence in waters just above the deep seafloor.

369 In comparison with GH's value (3), DWF's (6) is two orders of magnitude larger. Where GH is
370 quasi-permanent, DWF rarely occurs, for example not at all during the presented 20 months of
371 observations. Two orders of magnitude difference implies occurrence of (6) during one month per 8
372 years to match (3). This is the estimated maximum at a given site.

373 In comparison with mainly sub-mesoscale and internal-wave induced year-average value (4), DWF's
374 (6) would have to occur during 2.5 months per 8 years, or during 9 days every year. This is not observed
375 in the open Liguro-Provençal basin. It implies that, either DWF turbulence is stronger than (6) also for
376 $z < -2000$ m, which seems unlikely, or GH turbulence and especially SW turbulence are several times,
377 SW turbulence up to one order of magnitude, larger than DWF turbulence, when averaged over a decade
378 in time. With their sources of sub-mesoscale eddies and near-inertial waves, the warm SW conditions
379 thus seem more important than DWF for supply of fresh materials in the deep-sea area. Recall that the
380 observations are made in an area where tides, normally about half the ocean's mechanical energy source,
381 are weak.

382 The observed yearlong mean turbulence dissipation rate value of SW being 2.5 times that of GH in
383 the present area is the reverse of findings by Ferron et al. (2017), who find three times larger GH than
384 SW from sparse microstructure profiling across the entire Northwest Mediterranean. The discrepancy
385 may have to do with the location of the large-ring mooring, about 5 km from the foot of the continental
386 slope and most likely under the well-stratified boundary current most of the time.

387 Estimating turbulence dissipation rates from the microstructure profiler plots in Ferron et al. (2017)
388 gives average values for $h = 100-600$ m (the instruments were stopped some 90 m above the seafloor)
389 of about $2.5 \times 10^{-10} \text{ m}^2 \text{ s}^{-3}$ and $7 \times 10^{-10} \text{ m}^2 \text{ s}^{-3}$, for the Western Mediterranean and specifically Ligurian
390 Sea, respectively. These values are in the same range as mean and SW values (4) and (5), respectively.
391 Both averaged microstructure profiles showed reduction in values in the lower $h = 100-200$ m to about
392 $1 \times 10^{-10} \text{ m}^2 \text{ s}^{-3}$ and $3 \times 10^{-10} \text{ m}^2 \text{ s}^{-3}$, respectively. For properly processed microstructure profiler data the
393 instrumental error is to within a factor of two for mean turbulence dissipation rate values, not considering



394 environmental variations. The shown values, from the same height above seafloor as the upper range of
395 the moored T-sensors, compare with the GH-(3) and mean-(4) values determined at the large-ring
396 mooring.

397 A contribution of salt to density variations may possibly affect the turbulence values calculated from
398 the moored T-sensors under SW conditions, but density-temperature relationship across stratified layers
399 is found consistent between different years (van Haren, 2025). Also, convection turbulence under SW
400 conditions has been observed in deep alpine-lake Garda where salt contributes little to density variations
401 (van Haren and Dijkstra, 2021).

402 The relative importance of stratified turbulence occurring in varying strength over about half the time
403 has consequences for deep-sea transport, redistribution of matter and life. The regular replenishment is
404 partially related with atmospheric disturbances, in an indirect way. Winds do not directly affect motions
405 near the 2500-m deep seafloor. However, wind-induced near-inertial internal waves and boundary-
406 current variations affecting sub-mesoscale eddies seem to have correspondence with turbulence intensity
407 variations close to the seafloor, roughly a week after variations occur near the surface. More SW activity
408 and about 20% larger turbulence dissipation rates were found in winter when atmospheric activity was
409 correspondingly larger. Weakest stratification was found more in summer. As eddies and near-inertial
410 waves cause convection in the direction of the rotational axis to slant to the vertical under weak z-
411 direction stratification $N = O(f)$, cf. McEwan (1973); Straneo et al. (2002); Sheremet (2004); Gerkema
412 et al. (2008), the turbulence may come from above and in part horizontally.

413 In between stratified turbulence periods, waters tend to become near-homogeneous whilst being
414 dominantly mixed by convection turbulence through GH. As in Rayleigh-Taylor convection, plumes of
415 GH-response in waters overlying the seafloor strongly vary with time, and thus spatially (e.g., Dalziel
416 et al. 2008; Ng et al., 2016).

417 Geologically, even over a nearly flat sedimented seafloor underlying crustal cracks may develop
418 variable GH over distances as small as <1 km, depending on location of faults (e.g., Kunath et al., 2021).
419 This could explain observed variation in mean turbulence dissipation rates over the 70-m size of the
420 large-ring mooring, during GH. The 0.6-m high steel tubes of the large ring will not affect GH up to h



421 = 125 m. An inconclusive variation of mean turbulence values over periods of SW conditions
422 demonstrates larger scale variability.

423 Overall, the 45 vertical lines and nearly 3000 high-resolution T-sensors provided improved statistics
424 for daily mean turbulence dissipation rate values to within a reduced relative error of about 25%. Other
425 strengths of the mooring-array like improved spectral resolution and 3D evolution of turbulence will be
426 reported elsewhere, while short movies of 3D turbulence passages have been described in van Haren et
427 al. (2026).

428

429 *Data availability.* Only raw data are stored from the T-sensor mooring-array. Analyses proceed via
430 extensive post-processing, including manual checks, which are adapted to the specific analysis task.
431 Because of the complex processing the raw data from the custom-made T-sensors are not made publicly
432 accessible. Current meter and CTD data are available from van Haren (2025): “Large-ring mooring
433 current meter and CTD data”, Mendeley Data, V1, <https://doi.org/10.17632/f8kfwcvtdn.1>. Atmospheric
434 data are retrieved from <https://content.meteoblue.com/en/business-solutions/weather-apis/dataset-api>.

435

436 *Competing interests.* The author has no competing interests.

437

438 *Acknowledgments.* This research was supported in part by NWO, the Netherlands organization for the
439 advancement of science. Captains and crews of R/V Pelagia are thanked for the very pleasant
440 cooperation. NIOZ colleagues notably from the NMF department are especially thanked for their
441 indispensable contributions during the long preparatory and construction phases to make this unique
442 sea-operation successful. I am indebted to colleagues in the KM3NeT Collaboration, who demonstrated
443 the feasibility of deployment of large three-dimensional deep-sea research infrastructures. E. Berbee, P.
444 Kooijman, E. de Wolf, and E. Koffeman showed steep learning curves.

445



446 **Appendix A1 Layout of large-ring mooring**

447 The large-ring mooring has a diameter of nearly 70 m (Fig. A1). The eighteen 12-m long and 0.6-m
448 diameter steel tubes hold a steel-cable grid for rigidity. The cables are 9.5 m apart. At cable-intersects,
449 2.5-m diameter ‘small’ rings are mounted that each held a 125-m long mooring line with 65 T-sensors
450 below a single 1.45-kN buoy. Of eight small rings, imaginary intersects were at the steel tubes, so that
451 special off-set mounting was needed with three assist cables (van Haren et al., 2021). Upon landing at
452 the seafloor following parachute-controlled ‘free’ fall, the orientation of the ring was directed to the
453 NNW, pointing at 337 °N. After underwater chemical release of the buoys, the cable-grid was lifted in
454 a dome with its center $h = 2.0$ m above seafloor (van Haren, 2026 submitted).

455 The vertical mooring lines were named in six synchronisation groups, of maximum eight lines each.
456 The single synchroniser was located at the small ring of central line 51. Every half hour, the synchroniser
457 sent a clock pulse to a group. The synchronisation sequence of six pulses was repeated every four hours.
458



459 **Appendix A2 Proposed generalization of filter cut-off to compute Ellison scales**

460 Data from moored strings of high-resolution temperature sensors are potentially useful to compare two
461 different manners of calculating turbulence values. The more common method proposed by Thorpe
462 (1977) involves the reordering or sorting of unstable density overturns and the bookkeeping of their
463 vertical displacements, for vertical profiles at each time step. Turbulence values are computed following
464 averaging in the vertical, in time, or both and should include the largest of overturn scales. The method
465 requires a consistent temperature-density relationship. In near-homogeneous waters, difficulties may
466 arise in establishing such a relationship, but also in determining the size of largest overturns when they
467 outgrow the height of the string. A method is proposed to correct over-estimation under convection
468 turbulence by GH using verification via results from geophysical sampling (van Haren, 2025). In well
469 stratified waters, the Thorpe (1977) method has been successfully compared (e.g., Itsweire, 1984;
470 Moum, 1996; Cimatoribus et al., 2014), with results from the method introduced for atmospheric data
471 by Ellison (1957). In this Appendix, such a comparison is done for weakly stratified waters. A
472 modification is proposed of the Ellison (1957) method for application to data from moored instrumented
473 strings, and which is practically based on instrument performance and environmental physics conditions.

474 Ellison (1957) separated time series of potential temperature $\theta(t, z)$, which is dynamically equivalent
475 to Conservative Temperature Θ (IOC et al., 2010) in the ocean, at a fixed vertical position z in two,

$$476 \quad \theta = \langle \theta \rangle + \theta', \quad (A1)$$

477 where $\langle \cdot \rangle$ denotes the lpf series and the prime its hpf equivalent. If multiple sensors are deployed in the
478 vertical to establish a mean vertical gradient, a scale height can be defined as,

$$479 \quad L_E = \langle \theta'^2 \rangle^{1/2} / (d\langle \theta \rangle / dz). \quad (A2)$$

480 Itsweire (1984), using laboratory CTD-profile data, and Moum (1996), using ocean microstructure
481 profiler data, apply sorting as filter in z -direction. While their quasi-hpf data unlikely contain (linear)
482 internal waves, provided the profiles were instantaneously made and strictly vertical, they may contain
483 instrumental noise. With limited time-evolution available, it is assumed that the hpf data have worked
484 against the local stratification. The same assumption is made for Thorpe (1977) displacements. Sorting
485 works on all scales of overturns, which can be highly varying.



486 Like Thorpe-displacement ‘d’ scales, the Ellison scales of (A2) may be compared with the Ozmidov
487 (1965) scale $L_O = cL_E$ of largest possible turbulent overturns in stratified waters, so that the turbulence
488 dissipation rate reads,

$$489 \quad \varepsilon_E = c^2 L_E^2 N^3, \quad (A3)$$

490 in which the constant c needs to be established. If we take an average value of $c = 0.8$ (Dillon, 1982),
491 like commonly used for vertical root-mean-square ‘rms’ Thorpe scale $L_T = [d^2]$ so that $\varepsilon_T = c^2 L_T^2 N^3$, one
492 can compare average dissipation rate values between the two methods.

493 While the Thorpe (1977) method is most sensitive to proper resolution of the largest vertical overturn
494 scale, and the stratification (or buoyancy frequency) it works against, determination of Ellison scales
495 from moored-sensor time series is most sensitive for the appropriate separation between internal waves
496 and turbulent motions (Cimatoribus et al., 2014). For data from instrumented strings under well-
497 stratified Northeast-Atlantic conditions, wavelet decomposition worked using an averaging scale of
498 about $2/N$ for the lpf in (A1). Under such conditions, instrumental flaws like short-term bias of T-sensor
499 data were minimal. However, such a determination of Ellison scales is not a straightforward task under
500 weakly stratified and near-homogeneous conditions like occurring in the deep Western Mediterranean.

501 First, because such conditions imply very small variations in temperature (density), time series
502 require lpf to remove instrumental noise.

503 Second, time series require hpf to remove internal waves and (sub-)mesoscale motions. While the
504 common internal-wave band is considered between ranges f and N , for well stratified waters $N \gg f$,
505 more complex inertio-gravity wave ‘IGW’ frequency ‘ ω ’ bounds [$\omega_{\min} < f$, $\omega_{\max} > N$], for large-scale mean
506 N , have to be considered in waters where $N = O(f)$, e.g. (LeBlond and Mysak, 1978; Gerkema et al.,
507 2008). Furthermore, while average large-scale stratification hampers turbulent overturns, internal-wave
508 straining separates small thin-layer stratification, with small-vertical-scale buoyancy frequency N_s , from
509 near-homogeneous layers, with minimum buoyancy frequency N_{\min} , which may carry ditto waves
510 extending beyond the mean- N IGW-bounds. At the low-frequency, sub-inertial side of the IGW-band
511 the rare N_{\min} may combine with sub-mesoscale motions. More importantly, at the high-frequency, super-
512 buoyancy side N_s may combine with turbulent overturns. If all relevant scales are resolved, a safe



513 separation frequency would thus be at overall maximum $N_{\max} = \max(\max(N_s))$, where the maximum
514 between brackets is determined for each profile. In practice, such a transition frequency between internal
515 waves and turbulence is not easily determined, because it requires the small scales to resolve relevant
516 L_O . Only in weakly stratified waters, L_O are $O(10)$ m, and resolution of 1-2 m scales should be sufficient.

517 Thus, under weakly stratified conditions, instrumental noise and short-term bias have to be corrected
518 in t - and z -direction, respectively. A practical solution that also eliminates internal waves and sub-
519 mesoscale motions, is application of a band-pass filter ‘bpf’ in t , an lpf and sorting in z so that per time
520 step (A2) reads,

$$521 \quad |\theta'_{\text{bpf}}| / (d\theta_{\text{sorted}}/dz),$$

522 to which sufficient averaging is applied. Noting that stratification varies over different scales by two
523 orders of magnitude, so that $N_s \approx 0-6f$, filter design discriminates between conditions of SW and NH.
524 Sharp, phase-preserving double-elliptic filters (Parks and Burrus, 1987) are designed following
525 inspection of temperature variance spectra (Fig. A2).

526 For SW, reasonable filter cut-offs are tuned for a 1.7-day period around day 308 by equating (A3) to
527 ε_T . SW’s lpf cut-off is fixed at 3000 cpd. The reference hpf cut-off frequency $\omega_{\text{hpf,ref}}$ appeared at a small
528 flat (0-)slope near the low end of turbulence buoyancy- $(\omega^{-7/5})$ and inertial-subrange $(\omega^{-5/3})$ slopes, where
529 a short steep slope to internal-wave frequencies occurred. For other SW-periods, reference is not made
530 using average large-scale N , but a better fit is found for the time average of maximum small-scale
531 buoyancy frequencies per profile $N_m = \langle \max(N_s) \rangle$ so that,

$$532 \quad \omega_{\text{hpf}}^{\text{SW}} = (N_m / N_{m,\text{ref}})^2 \omega_{\text{hpf,ref}} \quad (\text{A4})$$

533 For NH, the lpf cut-off is fixed at 500 cpd. For its hpf cut-off, a flat (0-) slope appeared at a frequency
534 just higher than ω_{\max} so that, independent of measured $\langle N_{s,\max} \rangle$ the cut-off is blocked at,

$$535 \quad \omega_{\text{hpf}}^{\text{NH}} = 3.7 \text{ cpd.} \quad (\text{A5})$$

536 This value is tuned for a period with dominant GH, for which the geophysics-determined (e.g., Pasquale
537 et al., 1996) buoyancy flux $fl / \Gamma_C = \varepsilon_{\text{GH}} = 1.2 \times 10^{-10} \text{ m}^2 \text{ s}^{-3}$. In the present (Fig. 6) and previous (van Haren,
538 2025) data the mixing coefficient was found to amount $\Gamma_C = 0.5$, which is typical for convection
539 turbulence (Dalziel et al., 2008; Ng et al., 2016).



540 The cut-off frequency in (A5) is to within ± 0.2 cpd equivalent to $1.8(2\Omega) \approx 1.8\langle\omega_{\max}\rangle \approx 2\langle N_{s,\max}\rangle$
541 $\approx 0.5\langle U\rangle/\langle L_T\rangle = 0.5\omega_o$, for the deep Western Mediterranean site. Ω denotes the Earth rotation, and U
542 the waterflow speed. The Ozmidov (1965) frequency ω_o is a natural separator between internal waves
543 and stratified turbulence. It is unknown why the filter cut-off is close to half the Ozmidov frequency.
544 Also puzzling is the lack of correspondence between (A4) and ω_o , with the factor varying between 0.3
545 and 0.9 for different periods of SW. In part this may have to do with the waterflow being measured at h
546 $= 126$ m, below which it may be more uniform under NH- than under SW-conditions.
547 As shown in Fig. 4 for (A4), and Fig. 5 for (A5), the comparison works well to within about 20%.
548 For Fig. 4, $\langle[\varepsilon_T]\rangle = 6.3\times 10^{-10} \text{ m}^2 \text{ s}^{-3}$ and $\langle[\varepsilon_E]\rangle = 6.7\times 10^{-10} \text{ m}^2 \text{ s}^{-3}$. For Fig. 5, $\langle[\varepsilon_T]\rangle = 2.0\times 10^{-10} \text{ m}^2 \text{ s}^{-3}$
549 and $\langle[\varepsilon_E]\rangle = 1.3\times 10^{-10} \text{ m}^2 \text{ s}^{-3}$. Further tests were performed for about ten 1-4 day periods of NH and
550 SW, and all were within above error, provided that the data post-processing was carefully done and
551 longer periods were avoided. Especially (A5) is very sensitive to small changes in filter steepness around
552 the cut-off frequency, presumably due to its proximity to the IGW upper bound.
553



554 **References**

- 555 Adrián-Martinez, S. et al.: Letter of intent for KM3NeT 2.0, *J. Phys. G*, 43, 084001, 2016.
- 556 Brainerd, K. E., and Gregg, M. C.: Surface mixed and mixing layer depths, *Deep-Sea Res. I*, 42, 1521-
557 1543, 1995.
- 558 Cimatoribus, A. A., van Haren, H., and Gostiaux, L.: Comparison of Ellison and Thorpe scales from
559 Eulerian ocean temperature observations, *J. Geophys. Res.*, 119, 7047-7065, 2014.
- 560 Crepon, M., Wald, L., and Monget, J. M.: Low frequency waves in the Ligurian Sea during December
561 1977, *J. Geophys. Res.*, 87, 595-600, 1982.
- 562 Dalziel, S. B., Patterson, M. D., Caulfield, C. P., and Coomaraswamy, I. A.: Mixing efficiency in high-
563 aspect-ratio Rayleigh-Taylor experiments, *Phys. Fluids*, 20, 065106, 2008.
- 564 Dickson, R. R., Lazier, J. R. N., Meincke, J., Rhines, P., and Swift, J.: Longterm coordinated changes
565 in the convective activity of the North Atlantic, *Progr. Oceanogr.*, 38, 241-295, 1996.
- 566 Dillon, T. M.: Vertical overturns: a comparison of Thorpe and Ozmidov length scales, *J. Geophys. Res.*
567 87, 9601-9613, 1982.
- 568 Ellison, T. H., Turbulent transport of heat and momentum from an infinite rough plane, *J. Fluid Mech.*,
569 2, 456-466, 1957.
- 570 Eriksen, C. C.: Observations of internal wave refraction of sloping bottoms, *J. Geophys. Res.*, 87, 525-
571 538, 1982.
- 572 Ferron, B., Bouruet Aubertot, P., Cuypers, Y., Schroeder, K., and Borghini, M.: How important are
573 diapycnal mixing and geothermal heating for the deep circulation of the Western
574 Mediterranean? *Geophys. Res. Lett.*, 44, 7845-7854, 2017.
- 575 Gerkema, T., Zimmerman, J. T. F., Maas, L. R. M., and van Haren, H.: Geological and astrophysical
576 fluid dynamics beyond the traditional approximation, *Rev. Geophys.*, 46, RG2004, 2008.
- 577 Gregg, M. C.: Scaling turbulent dissipation in the thermocline, *J. Geophys. Res.*, 94, 9686-9698, 1989.
- 578 IOC, SCOR, and IAPSO: The International Thermodynamic Equation of Seawater – 2010: Calculation
579 and Use of Thermodynamic Properties, Intergovernmental Oceanographic Commission,
580 Manuals and Guides No. 56, UNESCO, Paris, 196 pp, 2010.



- 581 Itsweire, E. C.: Measurements of vertical overturns in a stably stratified turbulent flow, *Phys. Fluids*,
582 27, 764-766, 1984.
- 583 Kunath, P., Chi, W.-C., Berndt, C., and Liu, C.-S.: A rapid numerical method to constrain 2D focused
584 fluid flow rates along convergent margins using dense BSR-based temperature field data, *J.*
585 *Geol. Res. Solid Earth*, 126, e2021JB021668, 2021.
- 586 LeBlond, P. H., and Mysak, L. A.: *Waves in the Ocean*, Elsevier, New York, 602 pp, 1978.
- 587 Lilly, J. M., Rhines, P. B., Visbeck, M., Davis, R., Lazier, J. R. N., Schott, F., and Farmer, D.: Observing
588 Deep Convection in the Labrador Sea during Winter 1994/95, *J. Phys. Oceanogr.*, 29, 2065-
589 2098, 1999.
- 590 Marshall, J., and Schott, F.: Open-ocean convection: Observations, theory, and models, *Rev. Geophys.*
591 37, 1-64, 1999.
- 592 McEwan, A. D.: A laboratory demonstration of angular momentum mixing, *Geophys. Fluid Dyn.*, 5,
593 283-311, 1973.
- 594 Mertens, C., and Schott, F.: Interannual Variability of Deep-Water Formation in the Northwestern
595 Mediterranean, *J. Phys. Oceanogr.*, 28, 1410-1424, 1998.
- 596 Moum, J. N.: Energy-containing scales of turbulence in the ocean thermocline, *J. Geophys. Res.*, 101,
597 14,095-14,109, 1996.
- 598 Ng, C. S., Ooi, A., and Chung, D.: Potential energy in vertical natural convection, *Proc. 20th*
599 *Australasian Fluid Mech. Conf.*, Paper 727, 4 pp.,
600 [https://people.eng.unimelb.edu.au/imarusic/proceedings/20/727 Paper.pdf](https://people.eng.unimelb.edu.au/imarusic/proceedings/20/727%20Paper.pdf), 2016.
- 601 Oakey, N. S.: Determination of the rate of dissipation of turbulent energy from simultaneous temperature
602 and velocity shear microstructure measurements, *J. Phys. Oceanogr.*, 12, 256-271, 1982.
- 603 Osborn, T. R.: Estimates of the local rate of vertical diffusion from dissipation measurements, *J. Phys.*
604 *Oceanogr.* 10, 83-89, 1980.
- 605 Ozmidov, R. V.: About some peculiarities of the energy spectrum of oceanic turbulence, *Dokl. Akad.*
606 *Nauk SSSR*, 161, 828-831, 1965.
- 607 Parks, T. W., and Burrus, C. S.: *Digital Filter Design*, John Wiley Sons, New York, 342 pp, 1987.



- 608 Pasquale, V., Verdoya, M., and Chiozzi, P.: Heat flux and timing of the drifting stage in the Ligurian–
609 Provençal basin (northwestern Mediterranean), *J. Geodyn.*, 21, 205-222, 1996.
- 610 Polzin, K. L., Toole, J. M., Ledwell, J. R., and Schmitt, R. W.: Spatial variability of turbulent mixing in
611 the abyssal ocean, *Science*, 276, 93-96, 1997.
- 612 Schott, F., Visbeck, M., Send, U., Fischer, J., Stramma, L., and Desaubies, Y.: Observations of deep
613 convection in the Gulf of Lions, northern Mediterranean, during the winter of 1991/ 92, *J. Phys.*
614 *Oceanogr.*, 26, 505-524, 1996.
- 615 Sheremet, V. A.: Laboratory experiments with tilted convective plumes on a centrifuge: A finite angle
616 between the buoyancy force and the axis of rotation, *J. Fluid Mech.*, 506, 217-244, 2004.
- 617 Steffen, E. L., and D’Asaro, E.: Deep convection in the Labrador Sea as observed by Lagrangian floats,
618 *J. Phys. Oceanogr.*, 32, 475-492, 2002.
- 619 Straneo, F., Kawase, M., and Riser, S. C.: Idealized models of slantwise convection in a baroclinic flow,
620 *J. Phys. Oceanogr.*, 32, 558-572, 2002.
- 621 Thorpe, S. A.: Turbulence and mixing in a Scottish loch, *Phil. Trans. Roy. Soc. Lond. A*, 286, 125-181,
622 1977.
- 623 Thorpe, S. A.: Current and temperature variability on the continental slope, *Phil. Trans. Roy. Soc. Lond.*
624 *A*, 323, 471-517, 1987.
- 625 Thorpe, S. A.: *The turbulent ocean*, Cambridge Univ Press, Cambridge, 439 pp, 2005.
- 626 van Haren, H.: Abrupt transitions between gyroscopic and internal gravity waves: the mid-latitude case,
627 *J. Fluid Mech.*, 598, 67-80, 2008.
- 628 van Haren, H.: Philosophy and application of high-resolution temperature sensors for stratified waters,
629 *Sensors*, 18, 3184, doi:10.3390/s18103184, 2018.
- 630 van Haren, H.: Thermistor string corrections in data from very weakly stratified deep-ocean waters,
631 *Deep-Sea Res. I*, 189, 103870, 2022.
- 632 van Haren, H.: Corrected values of turbulence generated by general geothermal convection in deep
633 Mediterranean waters, *Ocean Dyn.*, 75, 46, 2025.
- 634 van Haren, H., and Dijkstra, H. A.: Convection under internal waves in an alpine lake, *Env. Fluid Mech.*,
635 21, 305-316, 2021.



- 636 van Haren, H. and Gostiaux, L.: Detailed internal wave mixing observed above a deep-ocean slope, J.
637 Mar. Res., 70, 173-197, 2012.
- 638 van Haren, H., and Millot, C.: Seasonality of internal gravity waves kinetic energy spectra in the
639 Ligurian Basin, *Oceanol. Acta*, 26, 635-644, 2003.
- 640 van Haren, H., Bakker, R., Witte, Y., Laan, M., and van Heerwaarden, J.: Half a cubic hectometer
641 mooring-array 3D-T of 3000 temperature sensors in the deep sea, *J. Atmos. Ocean. Technol.*,
642 38, 1585-1597, 2021.
- 643 van Haren, H., et al.: Whipped and mixed warm clouds in the deep sea, *Geophys. Res. Lett.*, in press,
644 2026.
- 645 Yasuda, I., et al.: Estimate of turbulent energy dissipation rate using free-fall and CTD-attached
646 fast-response thermistors in weak ocean turbulence, *J. Oceanogr.*, 77, 17-28, 2021.
- 647

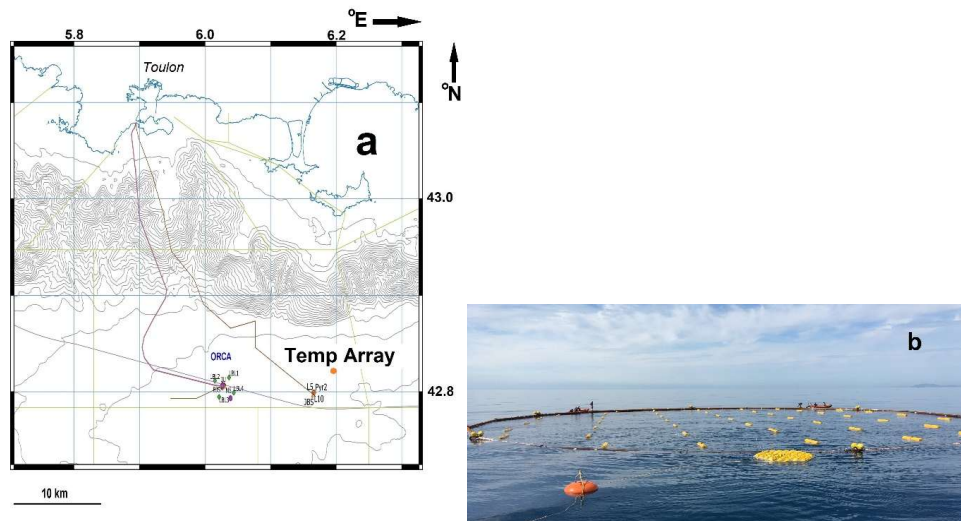


648 **Table 1.** General first and second moment statistics calculated for 45-line, 124-m height, and half-day
649 period turbulence dissipation rate values of Fig. 6. Two environmental conditions are characterized:
650 SW = stratified-water, NH = near-homogenous, and may include GH. The two conditions are
651 separated by a criterion equivalent of $N = 0.65f$.

652

653	<i>Day</i>	$\epsilon_T [m^2 s^{-3}]$	<i>Cond.</i>
654	308	$4.0 \pm 0.8 \times 10^{-10}$	SW
655	441	$1.5 \pm 0.1 \times 10^{-9}$	SW
656	459	$1.0 \pm 0.2 \times 10^{-10}$	NH
657	495	$1.0 \pm 0.2 \times 10^{-10}$	NH
658	485	$4.8 \pm 0.4 \times 10^{-10}$	SW
659	652	$1.4 \pm 0.1 \times 10^{-10}$	NH

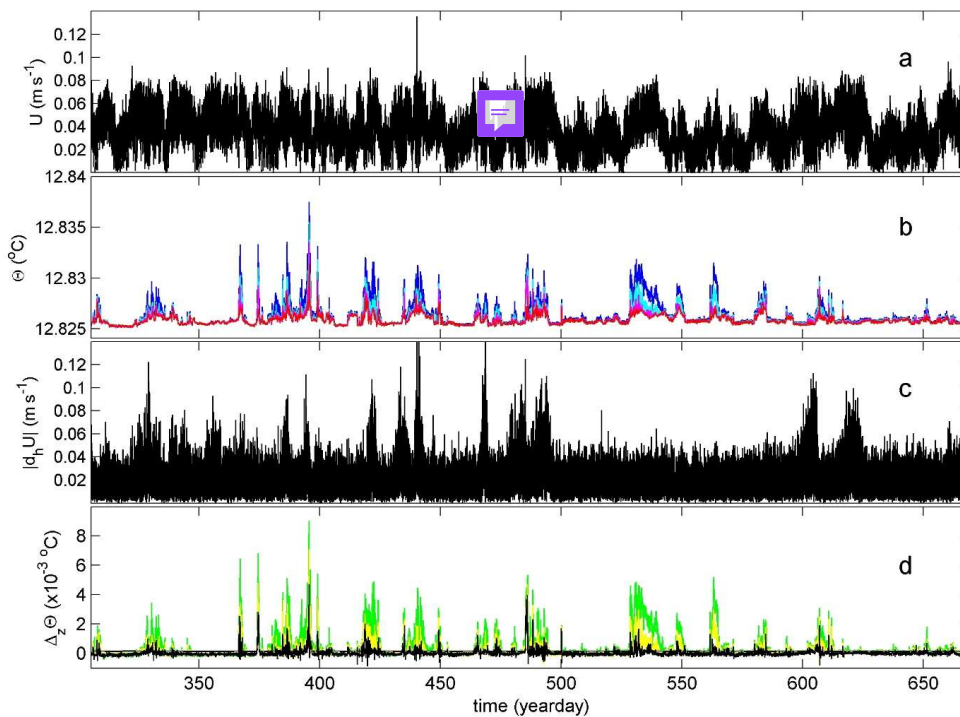
660



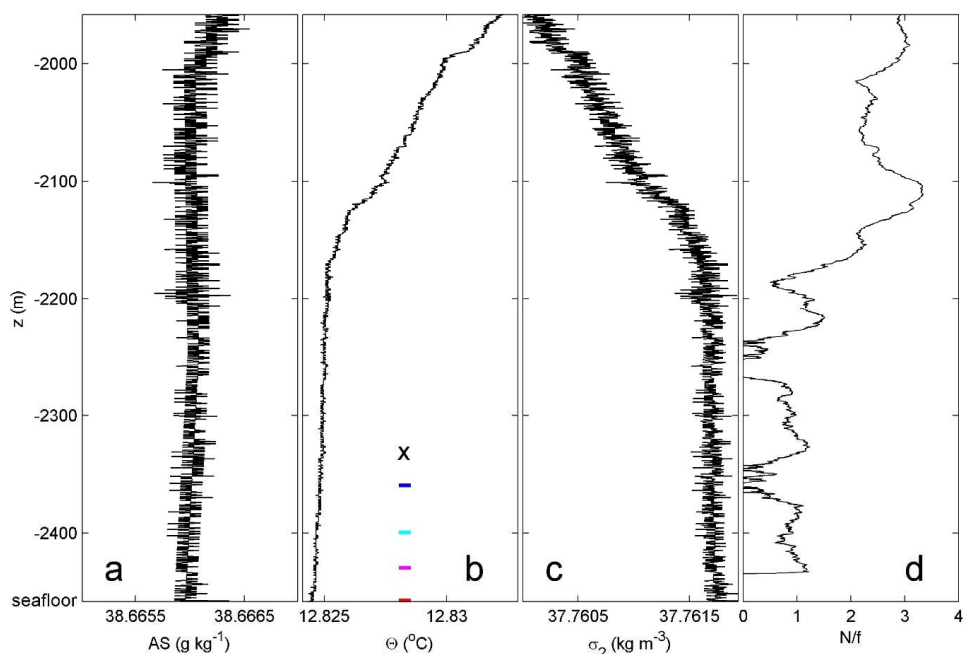
661

662 **Figure 1.** Large-ring mooring site and deployment. (a) Location named "Temp Array" (orange dot) on map
663 off southern France. The mooring is well east of main neutrino telescope 'NT' site "ORCA" of KM3NeT
664 (Adrián-Martinez et al., 2016) and just northeast of the former ANTARES NT-site. Isobaths are drawn
665 every 100 m. (b) At sea, during deployment finalizing the opening of air valves before sinking. The near
666 part of the large steel-tube ring is already underwater. Almost all buoys of the 45 small-ring compacted
667 vertical lines are visible (for layout see Appendix A1).

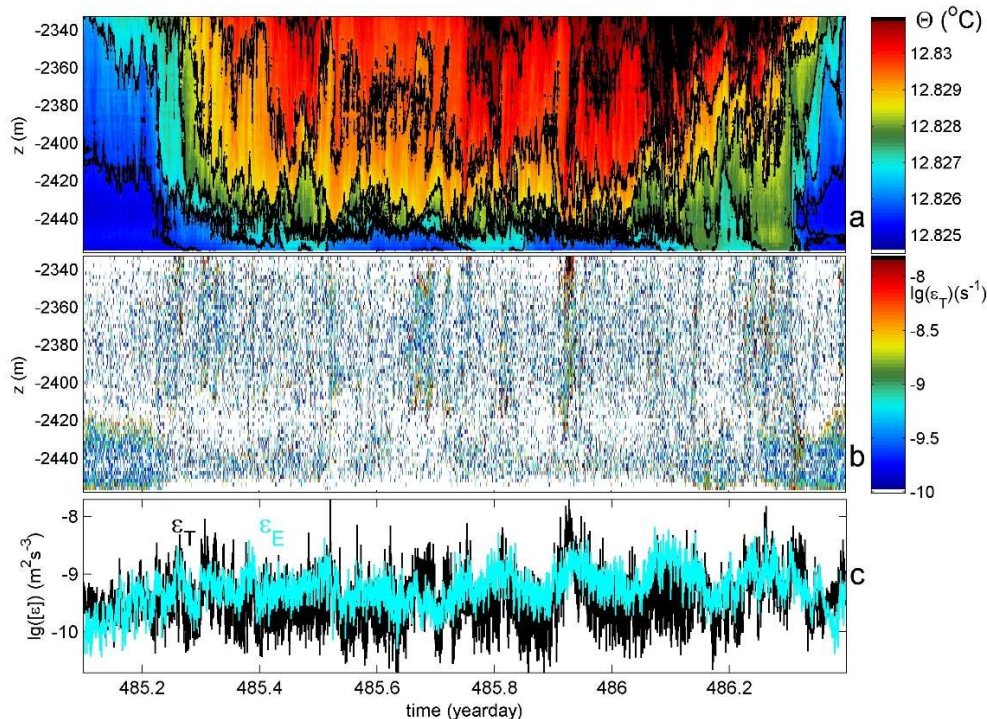
668



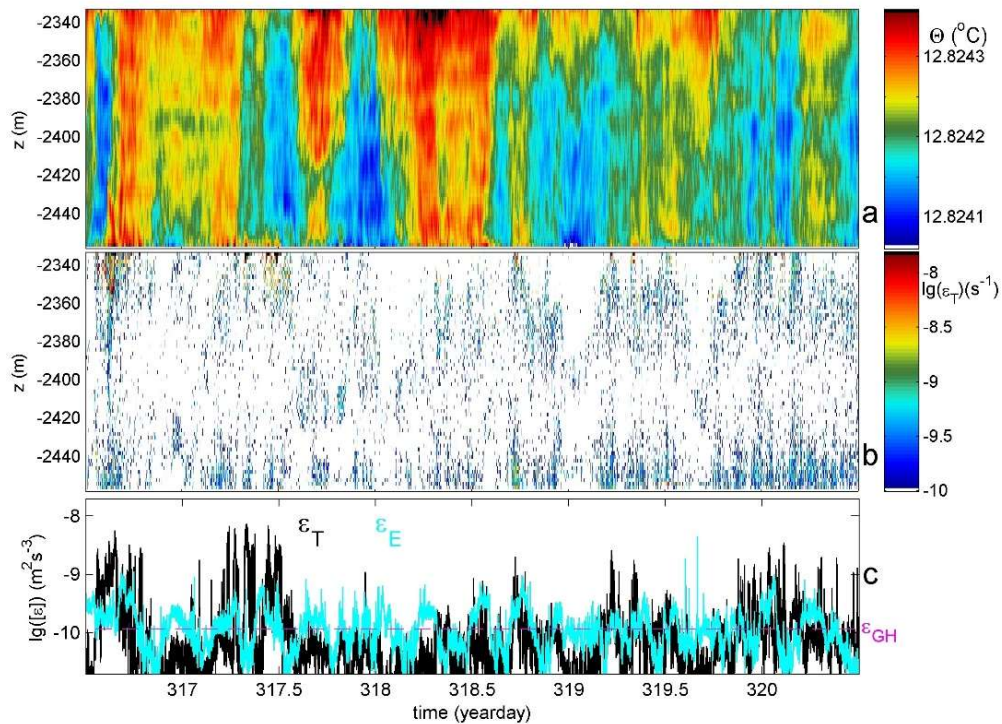
669
670 **Figure 2.** Time series of T-sensor and current meter ‘CM’ data, for the first year after deployment. Time
671 in days of year 2020, +366 in 2021. (a) Unfiltered waterflow speed at $h = 126$ m above seafloor. (b)
672 Conservative Temperature from vertical line 25, at $h = 1.5$ (red), 29.5 (magenta), 59.5 (cyan) and
673 99.5 m (blue), corrected for drift and referenced to CTD-data of Fig. 3b. (c) Amplitude of horizontal
674 flow differences. (d) Vertical temperature differences between the lowest T-sensor and those above
675 from b.



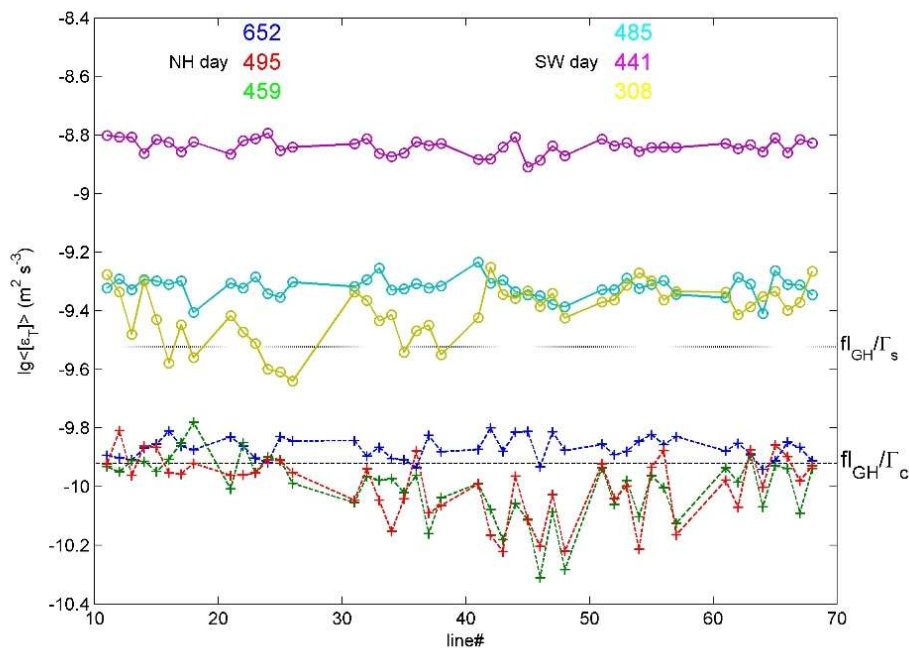
676
677 **Figure 3.** Lower 500 m of shipborne CTD profile obtained to within 0.5 m from the seafloor (at $z = -2458$
678 m). (a) Absolute Salinity, with x-axis range similar to that of b. in terms of contribution to density
679 variations. (b) Conservative Temperature. The colored ticks indicate the vertical positions of the four T-
680 sensors of which data are displayed in Fig. 2a. The 'x' indicates the position of CM. (c) Density anomaly
681 referenced to $2 \times 10^7 \text{ N m}^{-2}$. (d) Ratio of 25-m scale buoyancy frequency 'N' over local inertial frequency
682 'f'.
683



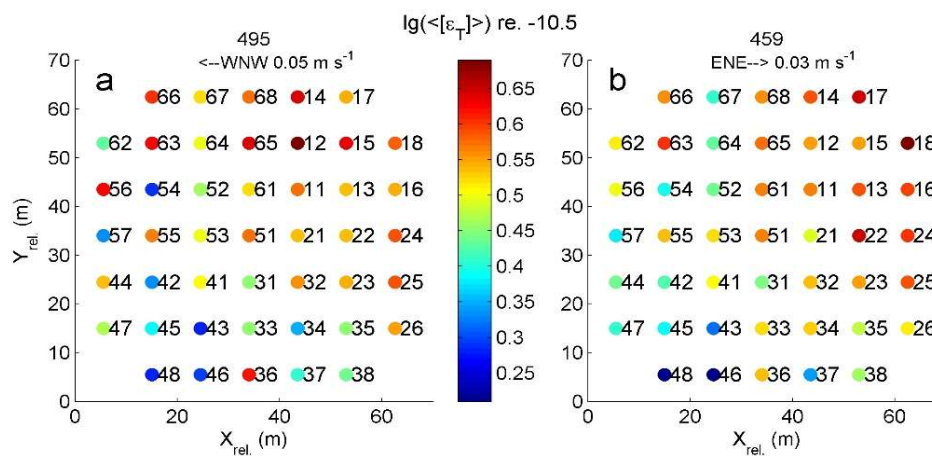
684
685 **Figure 4.** A 1.3-day period of relatively strong stratification with maximum small-scale buoyancy
686 frequency $N_{\max} = 6f$, for data from vertical line 15. (a) Time-depth plot of Conservative Temperature
687 with black contours every 0.001°C . The horizontal axis is at the seafloor. (b) Logarithm of non-averaged
688 turbulence dissipation rate from data in a. using Thorpe (1977) method. (c) Time series of logarithm of
689 data from b. averaged over 124-m vertical extent of T-sensors (black), compared with calculations using
690 Ellison (1957) method (cyan) with high-pass filter ‘hpf’ cut-off from Fig. A2a.
691



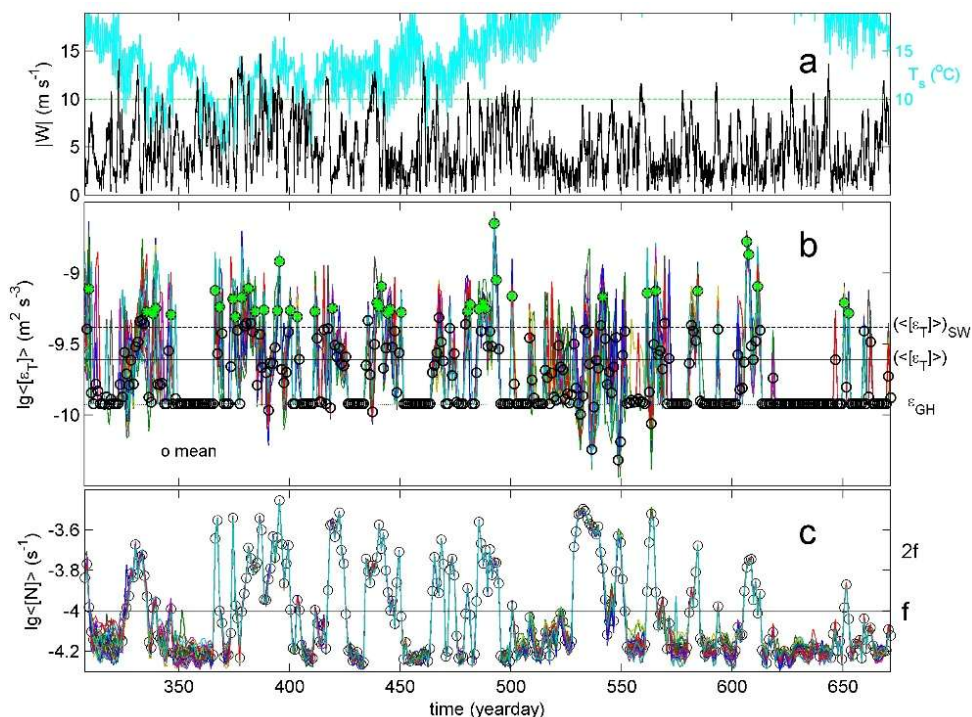
692
693 **Figure 5.** As Fig. 4, but for four days of near-homogeneous conditions with mean $N \approx 0.5f$, very weak
694 stratification alternated with convectively unstable periods. For c., the hpf cut-off for determining ϵ_E is
695 shown in Fig. A2b and the magenta-dashed line indicates the average dissipation rate attributed to
696 geothermal heating ‘GH’ (see text).
697



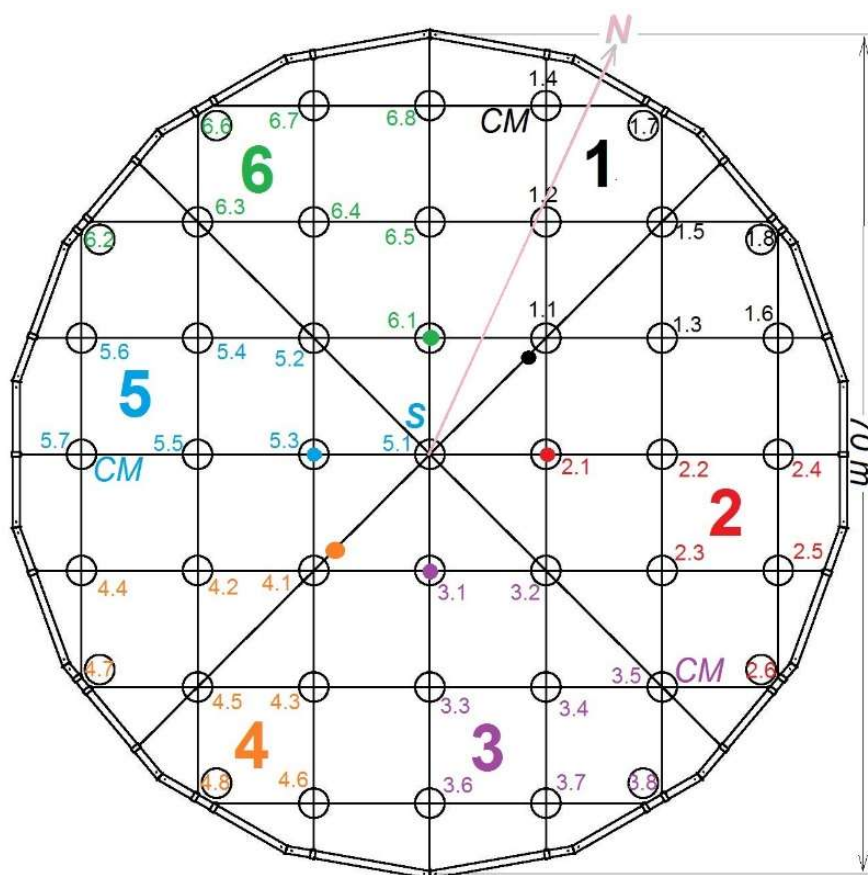
698
 699 **Figure 6.** Limited statistics of Thorpe (1977) method (logarithm of) turbulence dissipation rates averaged
 700 over 124 m vertically given for six 12-h periods indicated by day-number, as a function of all 45 lines
 701 that are indicated their number ‘line#’. Two thresholds are given as a function of general average
 702 buoyancy flux ‘fl’ from GH, divided by mixing coefficient for convection-turbulence $\Gamma_c = 0.5$ (Dalziel
 703 et al., 2008) and for shear-turbulence $\Gamma_s = 0.2$ (Osborn, 1980; Oakey, 1982). Solid lines (o) indicate
 704 Stratified-Water ‘SW’ conditions, dashed lines (+) indicate near-homogeneous ‘NH’ conditions.
 705



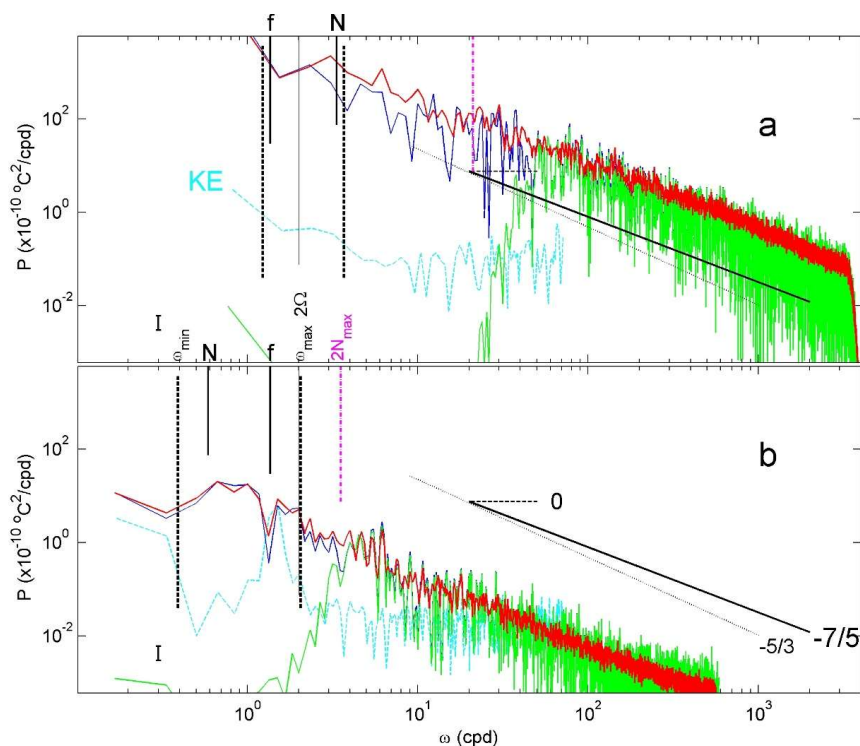
706
 707 **Figure 7.** Plan view of 4 lines indicating logarithm relative to a value of -10.5 of time- and vertical-mean
 708 turbulence dissipation rates for NH conditions on days 495 and 459 of Fig. 6. On top, half-day mean
 709 waterflows are indicated.
 710



711
 712 **Figure 8.** Yearlong time series of 45-line, daily, and vertically averaged turbulence and stratification values
 713 compared with meteorological data. (a) Wind speed (black) and surface temperature (cyan) measured at
 714 the station of Porquerolles Island, 20 km north of the mooring-array. The horizontal line is an arbitrary
 715 reference line below which near-surface convection may occur under sufficient pre-conditioning. (b)
 716 Logarithm of daily and 124-m vertically averaged Thorpe (1977) method turbulence dissipation rate for
 717 all 45 lines (colour), including their mean values (black, circles) of which those exceeding twice the
 718 overall mean value (green asterisks). A threshold of 0.0002°C is applied for $T(125)-T(1)$, below which
 719 values are forced to mean $\epsilon_{GH} = 1.2 \times 10^{-10} \text{ m}^2 \text{ s}^{-3}$, see text. The solid horizontal line indicates the overall
 720 mean value (4), the dashed line the mean (5) for periods under SW conditions. (c) Logarithm of
 721 corresponding mean buoyancy frequencies from reordered temperature profiles. The horizontal line
 722 indicates the local planetary inertial frequency.



723
724 **Figure A1.** Orientation and layout of the large-ring mooring, with steel-cable grid and small rings numbered
725 in six synchronisation groups with colour dots indicating group nodes and synchronier 'S' at line 51.
726 Here and elsewhere in the text, lines are indicated without period for short. Lines 14, 35 and 57 held a
727 waterflow current meter 'CM' at the buoy.
728



729
 730 **Figure A2.** Spectra demonstrating filter cut-off frequencies for Ellison (1957) method under SW and NH
 731 conditions. Data from line 15. Weakly smoothed (6 degrees of freedom, dof) low-pass filtered ‘lpf’
 732 spectra from a single T-sensor at mid-height (blue) with hpf version (green) is compared with
 733 moderately smoothed (100-dof) lpf spectrum over all 63 T-sensors (red). For comparison, the weakly
 734 smoothed (10-dof) kinetic energy ‘KE’ spectra are given (cyan; arbitrary vertical scale), averaged over
 735 the three CM. For reference, several frequencies and turbulence-range spectral slopes are given, see
 736 text. (a) SW period of Fig. 4, with filter cut-off following a scaling of time mean $\langle N_{\max} \rangle^2$ and lpf cut-
 737 off at 3000 cpd (cycles per day). (b) NH period of Fig. 5, with hpf cut-off fixed near $2\langle N_{\max} \rangle$ and lpf
 738 cut-off at 500 cpd.